International Journal of Fracture **71:** 345–363, 1995.

Fracture parameters for interfacial cracks: an experimental-finite element study of crack tip fields and crack initiation toughness

LIMING XU and HAREESH V. TIPPUR
Department of Mechanical Engineering, Auburn University, Auburn, Alabama 36849, USA

Received 14 December 1993; accepted in revised form 30 January 1995

Abstract. Crack tip measurements and analysis of interfacial parameters for PMMA-aluminum bimaterial system are presented. A variety of crack tip mode-mixities are obtained by subjecting asymmetric four-point-bend specimens to different boundary loads. The crack tip fields are mapped using the optical method of Coherent Gradient Sensing (CGS). The complex stress intensity factors and the associated crack tip mixities (ψ) are measured from CGS fringe patterns. The asymptotic expansion field for interface cracks is used for extracting fracture parameters by accounting for higher order contributions to the experimental data. The measurements are compared with complementary finite element computations. A linear relationship between crack tip mixity and the applied load mixity is experimentally demonstrated in this large elastic mismatch system. The fracture load and hence the energy release rate $G_{cr}(\psi)$ at crack initiation is measured as applied load mixities are varied. Limited discussion on the influence of surface roughness prior to bonding on the fracture toughness is included. Positive and negative shear on the crack plane produce different failure responses in this bimaterial system and the observed asymmetry is akin to the one predicted by the T&H model that includes crack tip nonlinearity.

1. Introduction

Bimaterial systems with large stiffness mismatch are encountered in several engineering applications. Typical examples include fiber reinforced composites, adhesive joints, microelectronic devices with layered structure, and so on. Performance of such 'inherently mixed-mode' systems greatly depend on the failure characteristics of weak interfaces. A theoretical framework for analyzing the mechanics of fracture of dissimilar material interfaces has been worked out in recent years [1,2] based on the so-called oscillatory singularity first presented by Williams [3], and subsequently enriched by many others including Rice and Sih [4], Erdogan [5], Malyshev and Salganik [6] and Comninou [7]. A resurgence in the interest for quantifying fracture behavior of bimaterial systems in terms of fracture toughness and crack tip mode-mixity is evident from the works reported in [8–19]. They include several numerical and experimental investigations on brittle fracture of interfaces. These works primarily address bimaterial fracture mechanics issues related to crack tip deformation modeling and developing testing methods or fracture specimens for evaluating interface fracture toughness. Results presented by Cao and Evans [8], Wang and Suo [9], Liechti and Chai [10], O'Dowd et al. [11] and Tippur and Ramaswamy [12], demonstrate the dependence of critical energy release rate on mode-mixity for elastic bimaterial interfacial cracks. Different test specimens for interface fracture testing are proposed by Williams [13], O'Dowd et al. [14], Liechti and Chai [10], Charalambidies et al. [15] and Tippur and Ramaswamy [12]. Interface crack tip fields have also been experimentally studied by Lu and Chiang [16] using photoelasticity,

Tippur and Rosakis [17] using CGS, and Liechti and Knauss [18] using interferometry. Global energy release rate evaluation methods have been advanced by Charalambidies et al. [19].

The local crack tip measurements play an important role in modeling interfacial crack tip behavior. They often assist in refining fracture models and testing methods. Thus far relatively few interfacial crack results deal with this aspect. Results reported in [12, 16, 17] use optical methods for local crack tip measurements, while [10] reports results obtained using hybrid interferometric NCOD measurements and finite element analysis. Other results typically use either boundary measurements and/or numerical analysis for interfacial crack modeling. In this paper complementary optical and finite element investigations dealing with interface crack tip fracture parameters evaluation over a wide range of applied load mixities are reported. Crack tip parameters are obtained by full-field, optical measurement of local elasto-optic effects and a detailed finite element analysis, *independently*. Firstly it provides a one-to-one comparison between the experimental measurements and finite element computations. Secondly, energy release rates at crack initiation and crack tip mixities are measured for two different surface roughnesses. Asymmetric four-point-bend bimaterial fracture specimens, originally proposed by Suresh et al. [20] for mixed-mode fracture testing of homogeneous materials, are used in the study. The crack tip fields are mapped using the technique of coherent gradient sensing (CGS). The interference patterns are subsequently analyzed and crack tip parameters are extracted. The present investigation takes into account non-singular stress contributions to the interfacial crack tip field in finite size specimens by using asymptotic expansion field. A relationship between the measured crack tip mixity and the applied load mixity is sought. A plane stress finite element analysis (FEA) with identical material mismatch and loading conditions is carried out. These computations are used in conjunction with interaction integral method [21] to obtain numerical counterparts of energy release rate and crack tip mixity. The FEA results are compared with optical measurements. The present investigation also provides supplemental experimental data for the ones reported using modified flexural specimens [12] (where energy release rate could not be partitioned by moment decomposition technique and beam theory). Further interfacial crack initiation under a wide range of mixities is investigated and fracture toughness is measured as a function of mixity. Nonlinear effects are seen to influence the symmetry of the toughness curve in addition to the simple phase shift observed in earlier investigations.

2. Coherent Gradient Sensing (CGS)

In this investigation the optical method of transmission CGS was used for mapping the interfacial deformations under a wide range of remote load mixities. The optical arrangement for transmission CGS is shown in Fig. 1(a). Briefly, the working principle of the method is as follows: A collimated laser beam is transmitted through a phase object in the region of interest. Subsequently, the object wave front undergoes a series of diffraction as it propagates through two Ronchi rulings G_1 and G_2 of pitch p (grating lines parallel to, say, x-axis). Note that the two grating planes are parallel and are separated by distance Δ along the optical axis. The square wave transmission profile of the gratings (chromium on glass master gratings with anti-reflection coatings, p=25 μm and Δ=30–60 mm have produced satisfactory results) result in a zero diffraction order and several odd diffraction orders. For the sake of simplicity consider diffraction orders E_0, E_{+1} and E_{-1} only. Here θ is the diffraction angle ($\theta \approx (\lambda/p)$). The diffracted wavefronts emerging from the grating G_2 are collected by the filtering lens and the spectral contents are displayed on the focal plane of the lens. A filtering aperture is used

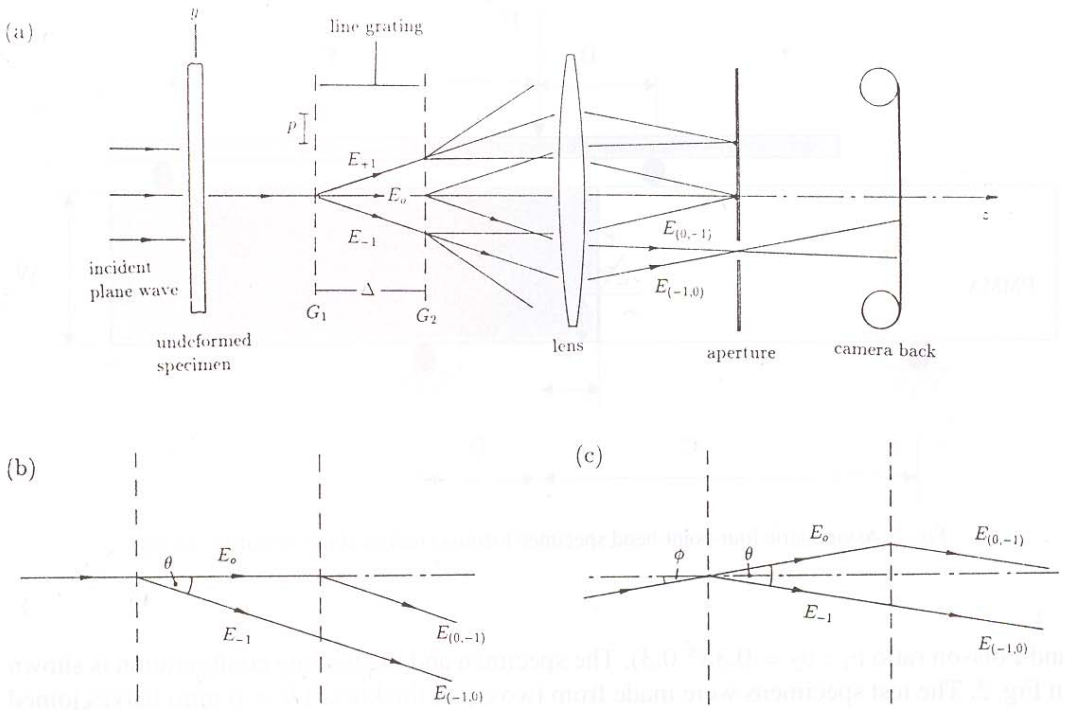

Fig. 1. (a) Optical arrangement for CGS set-up, (b) Wavefront shearing for undeformed object, (c) Wavefront shearing for deformed object.

to block all but $+1$ or -1 diffraction orders as shown (Fig. 1(b)). The filtered information produces laterally sheared object wave fronts on the image plane. Note that the recording arrangement consisting of the filtering lens and the camera back combination focussed on the object plane. The optics are arranged such that initially an uniform bright field or a bright fringe is observed on the image plane when the object is undeformed. Upon deformation light rays are deflected (Fig.1(c)) from the initial propagation direction parallel to the optical axis due to a combination of non-uniform changes in the refractive index (stress-optic effect) and the out-of-plane thickness change (Poisson effect) near the crack tip due to the imposed mechanical load. For transmission CGS, it is shown through diffraction analyses [22, 23] and a detailed Fresnel analysis [24] that mechanically induced warpage of the planar wave front can be related to in-plane gradients of $(\sigma_x+\sigma_y)$ where σ_x, σ_y are the normal thickness average stress components:

$$cB\frac{\partial(\sigma_x+\sigma_y)}{\partial y}=\frac{\mathcal{N}p}{\Delta}, \quad cB\frac{\partial(\sigma_x+\sigma_y)}{\partial x}=\frac{\mathcal{M}p}{\Delta}, \tag{1}$$

where c is the elasto-optic constant for the planar phase object, $\mathcal{M}$, $\mathcal{N}$ (=0, ±1, ±2, ...) are fringe orders, and B is the nominal thickness of the specimen.

3. Experiments and fringe analysis

Asymmetric four-point-bend bimaterial specimens were used in this study to obtain a wide range of mode-mixities. A material combination with a relatively large stiffness mismatch consisting of PMMA and aluminum was chosen (Young's modulus ratio $E_1 : E_2 = 1 : 24$

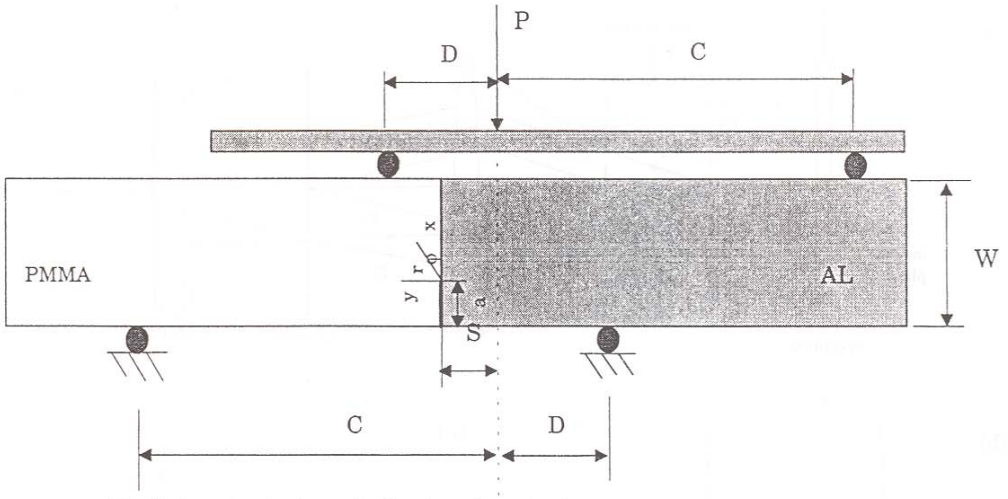

Fig. 2. Asymmetric four-point-bend specimen loading configuration ('negative' set-up).

and Poisson ratio $\nu_1 : \nu_2 = 0.35 : 0.3$). The specimen and the loading configuration is shown in Fig. 2. The test specimens were made from two equal thickness ($B = 6$ mm) halves joined by a two part adhesive – methyl-methacrylate monomer and a polymerizing agent (source: Weldon-10 manufactured by IPS Corp., Gardena, CA). Prior to bonding, the aluminum face of the interface was sand blasted and thoroughly cleaned to enhance bond strength (surface roughness $R_a = 4.3 - 4.5\mu$m). A thin Teflon tape insert was used to produce a sharp edge discontinuity of length a/W=0.33 along the interface where a and W denote the crack length and the specimen height, respectively. The bond was cured at laboratory temperature of 68 – 70°F for a period of 72–80 hours prior to testing. The resulting post-cure thickness of the bond material was approximately 50–100 μm. Before testing, each specimen was optically examined in the CGS set-up under no-load condition to ensure that the interface was free from initial fringe patterns representing residual stresses.

The bimaterial specimens were loaded in a displacement controlled loading device and the applied load P was measured using a load cell. Different far field mixities were introduced by varying the loading off-set distance s between the interface and the loading axis (see, Fig. 2). Note that when s=0, the crack plane is under to pure shear and increasing values of s result in increasing bending moment acting on the crack plane for the same magnitude of shear force when C and D are unchanged. Also, the configuration produced opening moment acting on the crack plane. Experiments were conducted for both 'positive' s and 'negative' s ($+s$ and $-s$ arrangements produce positive and negative shear on the crack plane, respectively). Note that the schematic in Fig. 2 corresponds to 'negative' s configuration (net shear force on the crack plane is in the $-x$ direction). Other relevant in-plane dimensions of the specimen were C/W=1.27 and D/W=0.63. The average shear and maximum normal stress acting on the crack plane for the configuration are given by,

$$\tau = \frac{P}{WB}\left(\frac{C-D}{C+D}\right), \quad \sigma = 6\tau\frac{s}{W}. \tag{2}$$

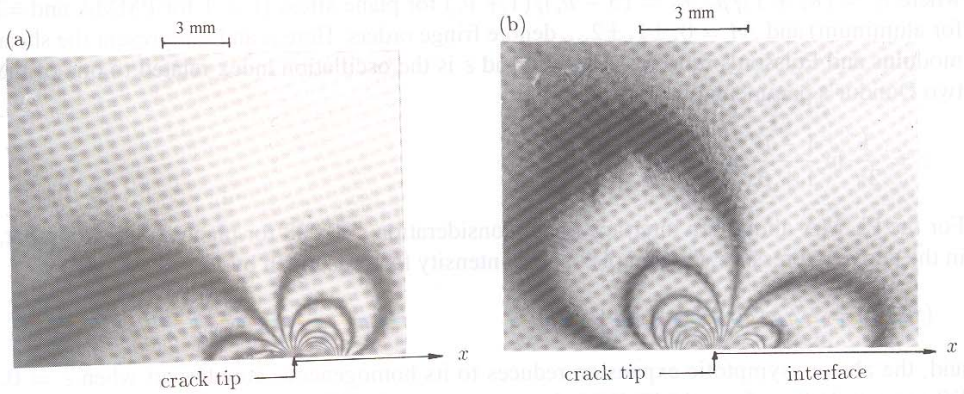

Fig. 3. Interference patterns representing contours of $\partial(\sigma_x + \sigma_y)/\partial x$ for (a) $s/W = -0$ ('negative' set-up), (b) $s/W = +0.33$ ('positive' set-up).

From the above, a measure of applied load mixity at a point on the crack plane can be introduced as, say, $\Theta = \tan^{-1}(\tau/\sigma) = \tan^{-1}(W/6s)$. Here, Θ is dependent on the eccentricity ratio (s/W) and is independent of C and D.

Transmission CGS technique was used for optical mapping of crack tip fields. The resulting interference patterns represent contours of $\partial(\sigma_x + \sigma_y)/\partial x$ in the PMMA half of the specimen. A 50 mm collimated He-Ne laser beam was transmitted through the specimen in the crack tip region. The interference patterns were recorded in real-time for different applied loads P. Experiments were conducted using master gratings of pitch p=0.025 mm and grating separation distance Δ=50 mm. Different s/W ratios varying from -0.5 to 0.5 (or, Θ was varied between $\pm 18°$ to $\pm 90°$) were used during the experiments. Typical interference patterns for two different values of $s/W = -0$ and +0.33 are shown in Fig. 3. The interference pattern represents an angular light deflection of 0.014 degree increment between successive fringes.

Considering the material above the interface ($0 < \phi < \pi$), and following Rice [1], the asymptotic expression for CGS fringes can be derived as given below

$$
\begin{aligned}
& cB\frac{\partial(\sigma_x + \sigma_y)}{\partial x} \\
& = 4cB\left(\sum_{n=1,3,5\ldots}^{\infty} e^{\varepsilon(\phi-\pi)} r^{(\frac{n}{2}-2)}\right. \\
& \quad \times\{A_n[(\tfrac{1}{2}n-1)\cos((\tfrac{1}{2}n-2)\phi - \varepsilon\ln(r/a)) + \varepsilon\sin((\tfrac{1}{2}n-2)\phi - \varepsilon\ln(r/a))] \\
& \quad + B_n[(\tfrac{1}{2}n-1)\sin((\tfrac{1}{2}n-2)\phi - \varepsilon\ln(r/a)) - \varepsilon\cos((\tfrac{1}{2}n-2)\phi - \varepsilon\ln(r/a))]\} \\
& \quad \left. + \sum_{n=2,4,6,\ldots}^{\infty} \frac{c_2}{c_1+c_2}(n-2) r^{(\frac{n}{2}-2)}[A_n\cos(\tfrac{1}{2}n-2)\phi + B_n\sin(\tfrac{1}{2}n-2)\phi]\right) \\
& = \frac{\mathcal{M}p}{\Delta},
\end{aligned}
\tag{3}
$$

where $c_i = (\kappa_i + 1)/\mu_i$, $\kappa_i = (3 - \nu_i)/(1 + \nu_i)$ for plane stress ($i = 1$ for PMMA and =2 for aluminum) and $\mathcal{M} = 0, \pm 1, \pm 2....$ denote fringe orders. Here μ and ν represent the shear modulus and Poisson's ratio respectively, and ε is the oscillation index related to one of the two Dundur's parameters (α, β)

$$\varepsilon = \frac{1}{2\pi} \ln \frac{1-\beta}{1+\beta} = \frac{1}{2\pi} \ln \frac{\mu_1 + \mu_2 \kappa_1}{\mu_2 + \mu_1 \kappa_2}.$$

For the PMMA-aluminum interface under consideration ε=0.098 for plane stress. Note that, in the above expression, the complex stress intensity factor is given by

$$(K a^{i\varepsilon}) = 2\sqrt{2\pi} \cosh(\pi\varepsilon)(A_1 + iB_1),$$

and, the above asymptotic expansion reduces to its homogeneous counterpart when $\varepsilon = 0$. When contributions from the higher order terms ($n > 1$ in (3)) are negligible compared to the dominant $n = 1$ term, the above equation can be approximated by

$$\begin{aligned} & cB \frac{\partial(\sigma_x + \sigma_y)}{\partial x} \\ & \approx \frac{cBr^{-3/2} e^{\varepsilon(\phi-\pi)}}{\sqrt{2\pi}\cosh(\pi\varepsilon)} \left[\{\mathrm{Re}(K a^{i\varepsilon})\} \left(-\cos\left(\frac{3\phi}{2} + \varepsilon \ln\frac{r}{a}\right) - 2\varepsilon \sin\left(\frac{3\phi}{2} + \varepsilon \ln\frac{r}{a}\right)\right) \right. \\ & \quad \left. + \{\mathrm{Im}(K a^{i\varepsilon})\} \left(\sin\left(\frac{3\phi}{2} + \varepsilon \ln\frac{r}{a}\right) - 2\varepsilon \cos\left(\frac{3\phi}{2} + \varepsilon \ln\frac{r}{a}\right)\right)\right] \\ & = \frac{\mathcal{M} p}{\Delta}. \end{aligned} \tag{4}$$

The mode-mixity using crack length as a scaling factor is

$$\psi(a) = \tan^{-1} \frac{\mathrm{Im}(K a^{i\varepsilon})}{\mathrm{Re}(K a^{i\varepsilon})}. \tag{5}$$

Next, the fringe patterns were digitized and fringe location (r, ϕ) and fringe order $(\mathcal{M})$ in the near tip region all around the crack tip were measured. Recognizing the existence of a region of dominant 3-D deformations near the crack tip [25], data in the region $(r/B \geqslant 0.5, 30° \leqslant \phi \leqslant 150°)$ near the crack tip was used in the analysis. To extract stress intensity factors from fringe patterns, overdeterministic least-squares data analysis was used. Also, in the analysis, K-dominant assumptions (4) were relaxed and higher order terms were incorporated in order to account for possible non-singular contributions to the field at distances beyond the anticipated 3-D zone. The procedure consists of minimizing the function $\Phi(r, \phi; A_1, B_1, A_2, B_2, ...)$,

$$\Phi = \sum_{i=1}^{M} w_i [F_i - F_i^{\mathrm{exp}}]^2, \tag{6}$$

with respect to the constants of the series A_n and B_n resulting in a system of linear algebraic equations of the form $\mathbf{A}x$=$\mathbf{b}$. Here F and F^{exp} are the right hand sides in (3), M denote the

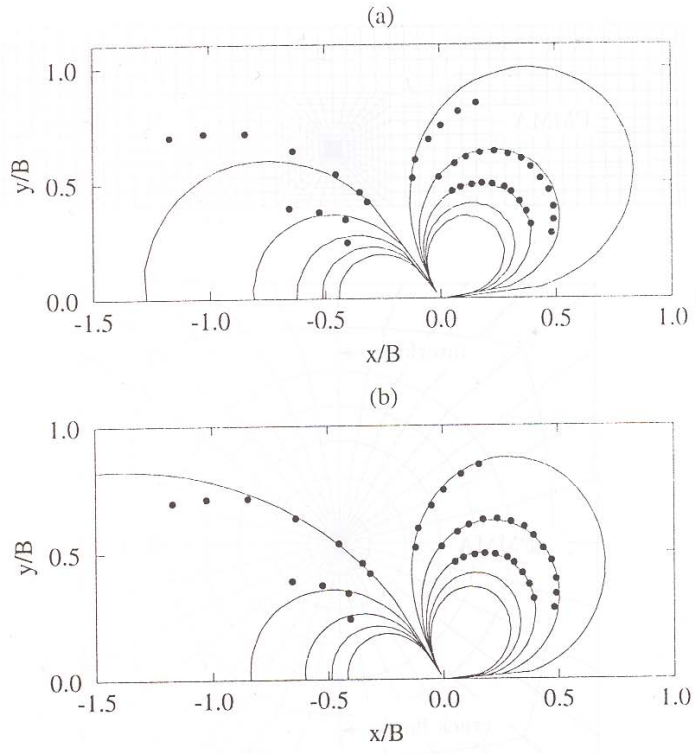

Fig. 4. Least-squares analysis of interference patterns ($s/W = -0$), (circles are measured data and lines are least-squares fit); (a) K-dominant analysis (Re($Ka^{i\varepsilon}$)=0.43 MPa$\sqrt{m}$, Im($Ka^{i\varepsilon}$)=-0.71 MPa$\sqrt{m}$, $\psi = -59°$), (b) Asymptotic field for $n = 4$, (Re($Ka^{i\varepsilon}$)=0.50 MPa$\sqrt{m}$, Im($Ka^{i\varepsilon}$)=-0.69 MPa$\sqrt{m}$, $\psi = -54°$).

total number of data points used in the analysis and w_i are the weighting factors. Also, in view of the asymptotic nature of the crack tip field in r, it is noteworthy that the matrix **A** obtained from the above method tends to be ill-conditioned when large number of higher order terms are included. In such cases, it is necessary to condition the matrix artificially by scaling the higher order coefficients in order to avoid unruly numerical fluctuations.

Each fringe pattern was first analyzed under the assumption of K-dominance. A typical result is shown in Fig. 4(a) for $s/W = -0$. The difference between the experimental data and the least-squares fit, particularly when $\phi > 90°$, suggests possible influence of non-singular stresses to the crack tip field and hence a need for including higher order terms in the least-squares analysis. In general, details of higher order contributions such as the number of higher order terms (n) to be used in the analysis and the relative importance of each term compared to others is unknown at the beginning of the data analysis. Hence, higher order contributions were included sequentially in the analysis until the match between the least-squares fit and the data was satisfactory and, stable values of Re($Ka^{i\varepsilon}$) and Im($Ka^{i\varepsilon}$) were attained. For example, Fig. 4(b) clearly shows an improvement in the correlation between the fit and the data when two higher order terms are included ($n = 4$ or, a total of five coefficients Re($Ka^{i\varepsilon}$), Im($Ka^{i\varepsilon}$), A_2, A_3, B_3). A systematic homogeneous counterpart of such an analysis can be found elsewhere [26].

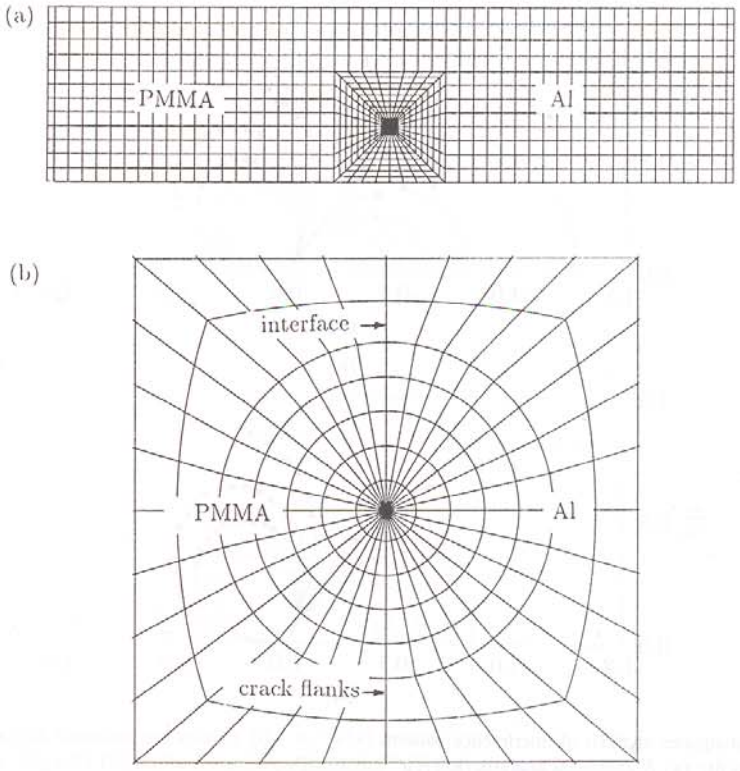

Fig. 5. Finite element model, (a) Complete model, (b) Near tip details.

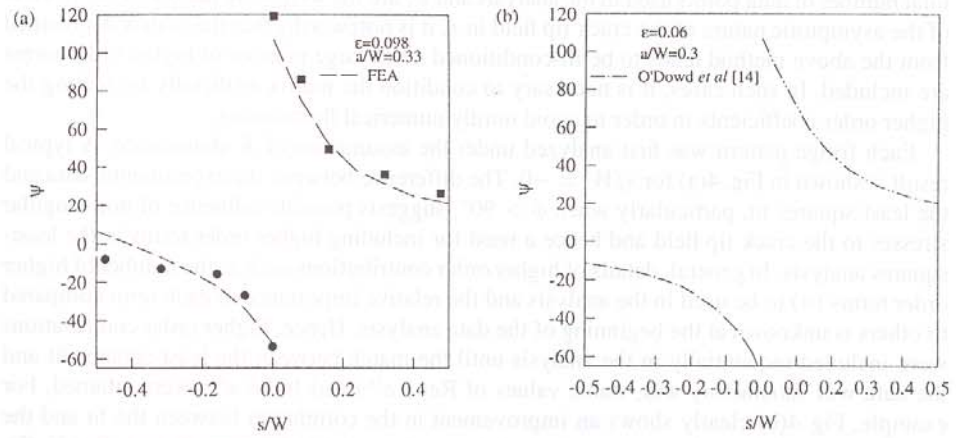

Fig. 6. (a) Comparison of optical measurement and finite element results of near tip mixity ψ for different s/W, (b) FE results from O'Dowd et al., [14].

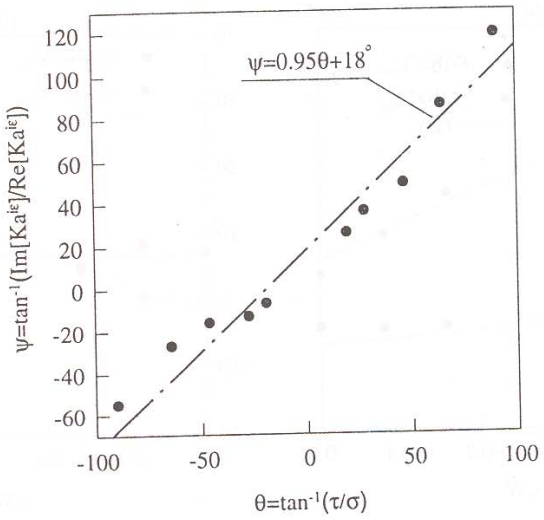

Fig. 7. Variation of near tip mixity ψ with applied load mixity Θ.

4. Finite element analysis

A complementary finite element analysis was carried out using ABAQUS^{TM} software package. The finite element model consisted of 1016 eight node plane stress elements and 3235 nodes (Fig. 5(a)). The crack tip region was discretized using a fine mesh with crack tip elements as small as $0.015a$, where a is the crack length. The near tip mesh is shown in Fig. 5(b). No attempt was made during the analysis to create any special type of singularity at the crack tip by using singular elements. The elements in the region $y > 0$ and $y < 0$ were assigned the material properties of PMMA (material-1) and aluminum 6061 (material-2) and the value of the oscillation index $\varepsilon = 0.098$. A crack length of $a/W = 0.33$ was kept constant while the loading eccentricity ratio s/W was varied in the range of $-0.5 \leqslant (s/W) \leqslant 0.5$. The other experimental parameters namely loading distances C/W=1.27 and D/W=0.63 were used in the finite element calculations. The finite element counterparts of Re$(Ka^{i\varepsilon})$, Im$(Ka^{i\varepsilon})$ and hence crack tip mixity ψ were obtained using the interaction energy release rate method proposed by Shih and Asaro [21] while the domain integral method was used for calculating different path independent integrals. Different domains surrounding the crack tip were investigated and the differences in the values were within 3 percent of each other. It should be noted that detailed FE results have been presented by O'Dowd et al. [14] for asymmetric bending geometry corresponding to an oscillation index $\varepsilon = 0.06$.

5. Results and discussion

5.1. Stress intensity factor and mode-mixity

Experimental measurements of crack tip parameters namely Re$(Ka^{i\varepsilon})$, Im$(Ka^{i\varepsilon})$ and ψ are compared with their finite element counterparts in Figs. 6–8. The variation of mixity ψ for the range $-0.5 \leqslant s/W \leqslant 0.5$ is shown in Fig. 6(a). The measurements (filled circles for 'negative' set-up and filled boxes for 'positive' set-up) are in good agreement with the finite

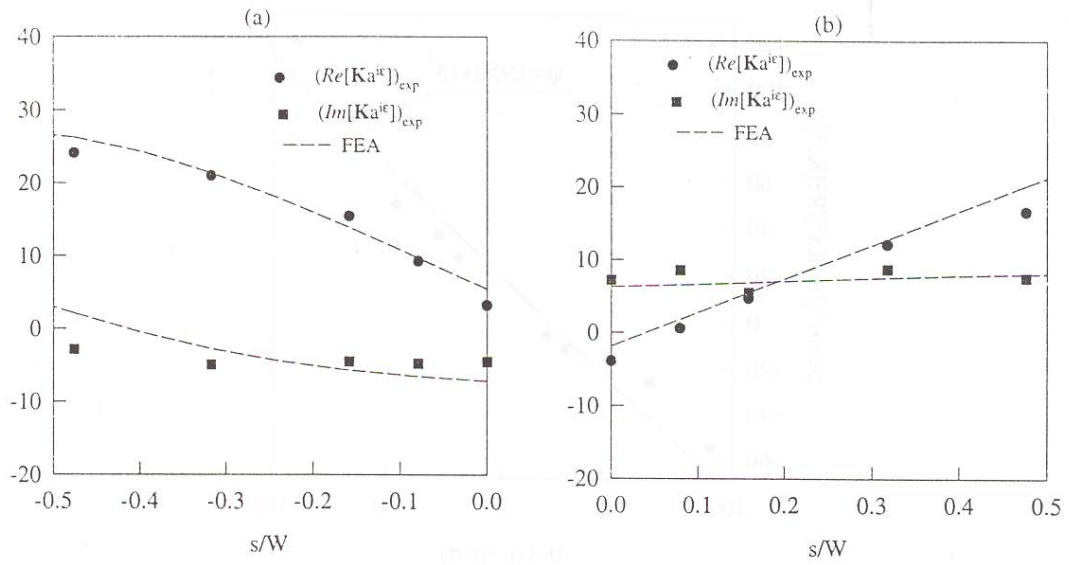

Fig. 8. Comparison of normalized stress intensity factors obtained from optical measurements and finite element computations for different s/W; (a) 'Negative set-up, (b) 'Positive set-up.

element results for both 'positive' and 'negative' set-ups. In the range $+0 \leqslant s/W \leqslant +0.04$ when the applied load is dominated by shear, the measured and the computed values of crack tip mixity exceed $\pi/2$ because of a negative $\mathrm{Re}(Ka^{i\varepsilon})$ and positive $\mathrm{Im}(Ka^{i\varepsilon})$. As s/W increases (positive set-up) ψ steadily decreases and seems to approach approximately 20° at large s/W. On the contrary, mixity corresponding to negative shear is approximately $-55°$ at $s/W = -0$ and again steadily approaches 0° at large s/W. These observations are similar to the numerical results presented by O'Dowd et al. [14] for a material mismatch parameter of $\varepsilon = 0.06$ and is shown in Fig. 6(b).

As pointed out earlier, one could interpret s/W ratio as an applied load mixity defined by $\Theta = \tan^{-1}(\tau/\sigma)$. For the range of experimental parameters used in the study, Θ varies from approximately $\pm 18°$ to $\pm$ 90°. In Fig. 7, crack tip mixity ψ is plotted as a function of the nominal mixity Θ on the crack plane. The measured values of ψ are shown as the discrete data points and they clearly suggest a linear relationship with Θ ($\psi = m_0\Theta + \psi_0$). This is an observation through direct crack tip measurements demonstrating a simple phase shift between interfacial crack tip mixity and the applied load mixity. Although such phase shifts are often suggested [2] for special cases with $\varepsilon \approx 0$ for simplifying the physical interpretation of interface stress intensity factors analogous to homogeneous counterparts, this is an experimental demonstration of the same even when ε is very large as in this case. The broken line represents a straight line fit through the data whose slope m_0 is approximately equal to 1 and the intercept $\psi_0 \approx 18°$. Note that ψ_0 is dependent on the material mismatch parameters and length scale which in this investigation is taken to be crack length a. The observed linearity in the range of s/W investigated suggests that if an alternative length scale $\hat{a} \approx 1.0 \times 10^{-3}$m is chosen instead of the current choice of $a = 25 \times 10^{-3}$m, it would make the crack tip mixity coincide with the applied load mixity *i.e.*, $\hat{\psi} = \Theta$ where

$$\hat{\psi} = \psi + \varepsilon \ln(\hat{a}/a).$$

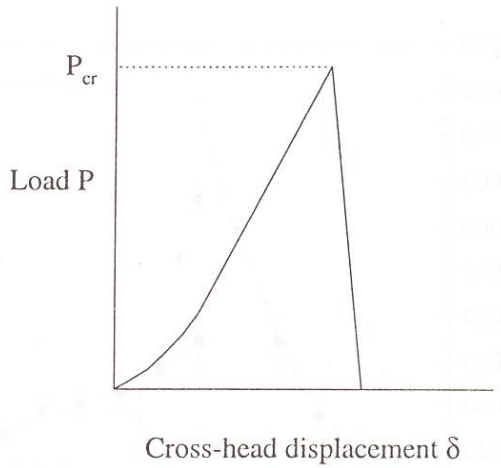

Fig. 9. Typical measured load vs. cross-head displacement record from failure load tests.

This would also simplify the interpretation of $\mathrm{Re}(K\hat{a}^{i\varepsilon})$, $\mathrm{Im}(K\hat{a}^{i\varepsilon})$, analogous to mixed-mode stress intensity factors in homogeneous material. If one knows $\hat{a}$ *a priori* in terms of Dundur's parameters and specimen dimensions or specimen geometry, the process of measuring crack tip mixity variation can be greatly simplified. In this direction, results for simple cases such as a centrally located crack lying on a bimaterial interface subject to remote tensile and shear stresses and, crack lying along the interface of two bimaterial strips held between rigid grips subject to different grip displacements are discussed in Hutchinson and Suo [2]. Also, it is noteworthy that $\hat{a} = 1.0 \times 10^{-3}$ m is beyond the Irwin plastic zone size for PMMA (which is of the order of 100 μm).

In Fig. 8(a,b), comparison of $\mathrm{Re}(Ka^{i\varepsilon})$ and $\mathrm{Im}(Ka^{i\varepsilon})$ from experimental measurements and FEA is presented. The stress intensity factors are normalized by $(P\sqrt{a}/W^2)$. Again the two results agree well with each other. In the entire range of s/W studied, $\mathrm{Im}(Ka^{i\varepsilon})$ is relatively constant while $|\mathrm{Re}(Ka^{i\varepsilon})|$ monotonically increases with $|s/W|$. This is due to a constant shear force being applied to the beam although s/W is varied. And, as discussed earlier, the measurements (Fig. 8(b)) estimate a negative $\mathrm{Re}(Ka^{i\varepsilon})$ when $+0 \leqslant s/W \leqslant +0.04$.

5.2. Interfacial fracture strength and toughness

Having demonstrated the ability of CGS for providing reliable interface crack tip measurements and the feasibility of the specimen for generating a wide range of mixities, we next discuss the interfacial fracture strength and crack initiation toughness testing of the bimaterial system. Specimens for these tests were prepared under conditions similar to the ones used in the optical study and as per the recommendation of the acrylic adhesive manufacturer. The aluminum halves of the specimens were sandblasted (particle size 5–15 μm) to increase the surface roughness ($R_a \approx 4.3$–4.5 μm) (and the surface area of contact) and hence an enhancement of the bond strength. The specimens were cured at room temperature for approximately 72–80 hours before testing. An edge crack was introduced in each specimen using a thin Teflon tape (thickness < 50 μm). The tests were conducted in an Instron universal testing machine at a constant cross-head displacement rate of 50 mm/min at room temperature. Specimens were loaded for different s/W ratios ranging from -0.5 to 0.5. Several specimens

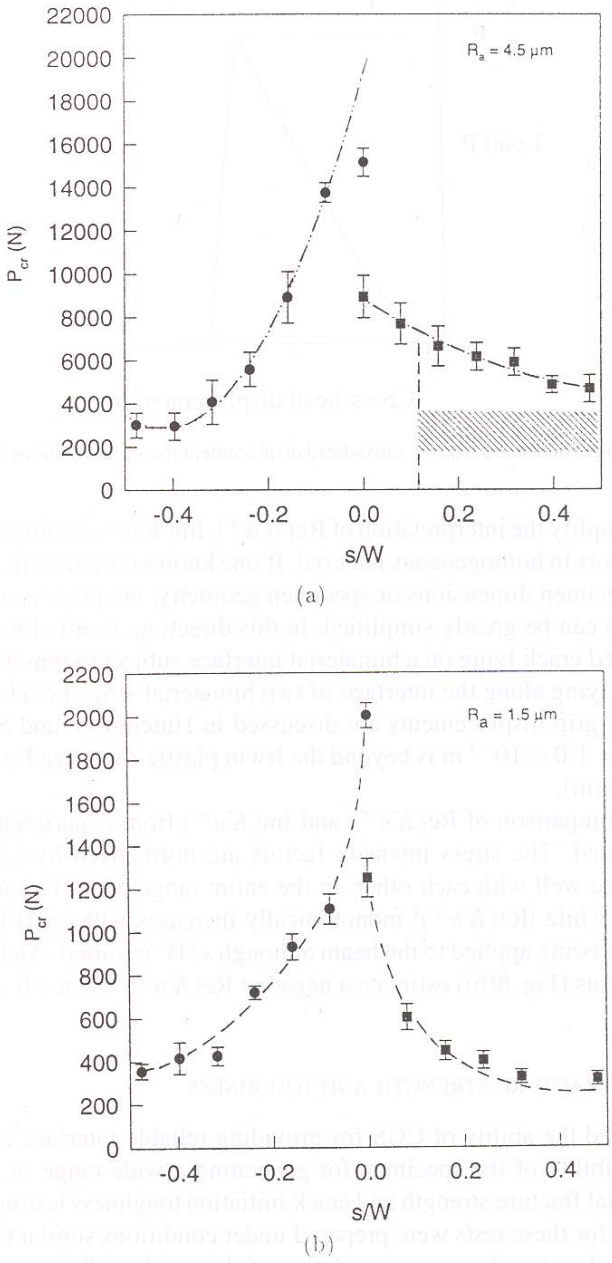

Fig. 10. Variation of fracture load P_{cr} for different applied load mixities. (a) Roughened aluminum surface, (b) As-machined aluminum surface prior to bonding.

were tested at each s/W ratio. A typical applied load vs. crosshead displacement ($P - \delta$) curve is shown in Fig. 9. The initial nonlinearity is due to the slack in the pin joints in the loading fixtures and the rest of the load-displacement history is essentially linear. The peak load was recorded as P_{cr} in each case and was observed to be close to the crack initiation

event. Note that P_{cr} is related to crack initiation toughness in this specimen configuration as $\mathrm{Re}(K\hat{a}^{i\varepsilon}) \propto f_1(s/W)P\sqrt{a}$ and $\mathrm{Im}(K\hat{a}^{i\varepsilon}) \propto f_2(s/W)P\sqrt{a}$. Explicit relations of the same can be found in [14]. Experimental evidence of the same will be discussed later in this section. The filled boxes in Fig. 10(a) correspond to the 'positive' set-up while filled circles correspond to the 'negative' set-up. When the applied shear on the crack plane was negative, the crack typically extended for small distances (3–10 mm) along the polymer-metal interface before branching into the PMMA. On the contrary, the crack remained on the polymer-metal interface when the applied shear was positive. The observation is consistent with the prediction of He and Hutchinson [27] who point out that conditions favor crack kinking into the less stiff material when a negative shear stress acts on the interface. In each test, the bond material had remained attached to the PMMA half of the specimen when macroscopically examined. When the specimens with $s/W = -0$ were examined, behind the crack front some evidence of surface rubbing was detected. A plot of P_{cr} as a function of s/W is shown in Fig. 10(a). The broken lines correspond to a smooth curve through the data and only suggest trends. Evidently the measured fracture loads seem to have a strong dependence on whether the crack plane shear is positive or negative in this bimaterial system. The value of P_{cr} is consistently higher for $s/W = -0$ when compared with the one for $s/W = +0$ (by a factor of at least 1.5). Moreover, P_{cr} variation between $s/W = +0$ and $+0.5$ is relatively small compared to the corresponding one between $s/W = -0$ and -0.5. The difference in P_{cr} values between $s/W = -0$ and $+0$ is due to the crack tip interpenetration when the interfacial plane is subjected to dominant shear loading. A theoretical study of the same for frictionless crack surfaces has been reported by Comninou and Schmueser [28] for interfacial cracks experiencing different combinations of normal and shear tractions. Similar phenomenon can also be seen in the present FE analysis. The deformed elements in the crack tip region are shown in Fig.11(a,b) for $s/W = -0$, and $= +0$, respectively. Note that the applied load for these computations correspond to the experimentally measured values of P_{cr} (from Fig. 10(a)). As is evident from the figure, the crack tip elements show interpenetration behind the crack tip when $s/W = -0$ and produce localized crack tip closure. The region of crack flank contact, however, seems to be confined to the first ring of elements surrounding the crack tip. On the other hand, $s/W = +0$ the crack tip elements do not show any interpenetration. But, the crack flanks are deformed such that they suggest crack flank rubbing due to surface roughness [29] at distances approximately $0.07a - 0.1a$. However, when the crack flank region was enlarged several times, the finite element model did not reveal physical contact between the two surfaces and the separation distance was much larger than the average surface roughness. Thus, the situation encountered here is relatively less severe when compared to the one observed when $s/W = -0$. A finite notch width used in the test specimens further alleviate the crack flank contact for $s/W = +0$. This is also consistent with lower P_{cr} values observed in these tests. Next, each of the fractured surfaces were examined in an optical microscope to identify events not readily evident to macroscopic examination. The aluminum half of the fractured surface ahead of the initial crack front in specimens corresponding to the shaded region of the s/W values in Fig. 10(a) showed evidence of fractured PMMA residue attached to the aluminum surface suggesting a rather complex crack path and in-layer fracture of the adhesive at crack initiation. A representative micrograph of such a fracture from the shaded region is shown in Fig. 12(a) for $s/W = +0.3$. It should be pointed out here that several specimens at each s/W ratio were tested in order achieve interfacial fracture rather than adhesive layer decohesion (Fig. 12(a)) and the attempts were consistently futile although P_{cr} values were reproducible. However, when fractured aluminum surfaces corresponding to s/W ratios in

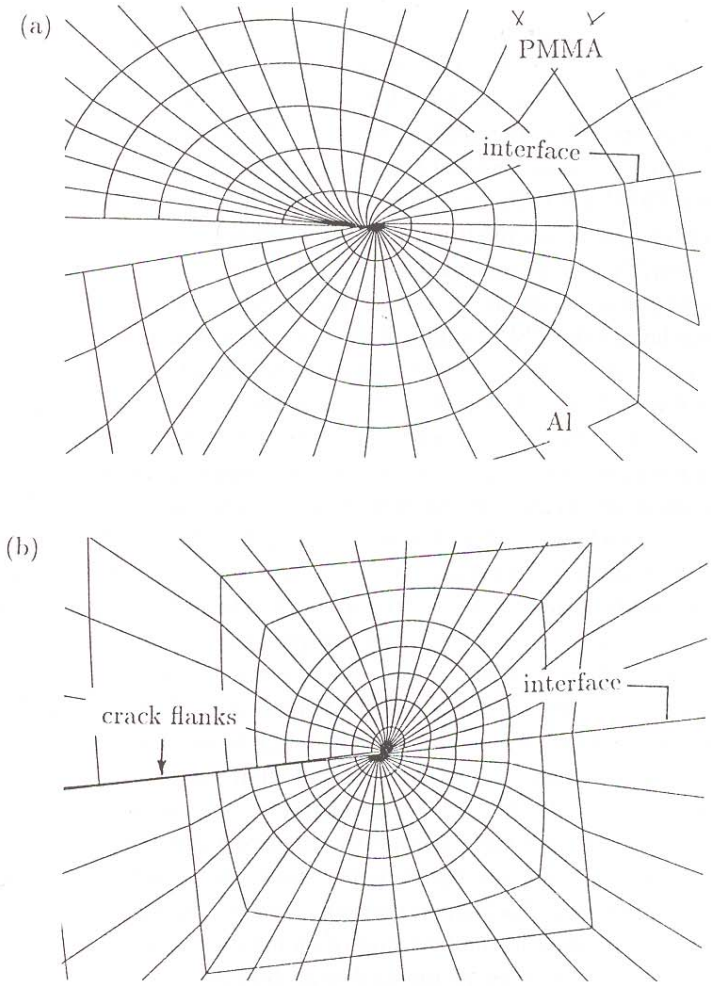

Fig. 11. Deformed near tip finite elements for (a) $s/W = -0$ and (b) $s/W = +0$.

the unshaded region of Fig. 10(a) were examined, a rather clean fracture without evidence of PMMA residue was observed. Figure 12(b) is a micrograph of the aluminum surface near the crack front for $s/W = -0.2$ and the surface texture corresponding to a roughened aluminum surface can be seen.

Some of the potential factors contributing to the in-layer fracture of the acrylic adhesive observed in the range $+0.15 < s/W < +0.5$ could be the local stress field, finite crack thickness and/or the roughness induced strength enhancement. Since Teflon tape of the smallest available thickness ($< 50\,\mu$m) has been used for producing the discontinuity, further reduction in the crack thickness for this adhesive could not be pursued. On the other hand, since the surface roughness could be experimentally controlled relatively easily, asymmetric four-point-bend interface specimens with a different surface roughness prior to bonding were prepared for measuring P_{cr} as a function of s/W. Some discussion on the toughness comparison between milled surfaces and polished surfaces prior to bonding in polymer-metal sandwiches has been reported by Wang and Suo [9] but no explicit relationship between roughness and

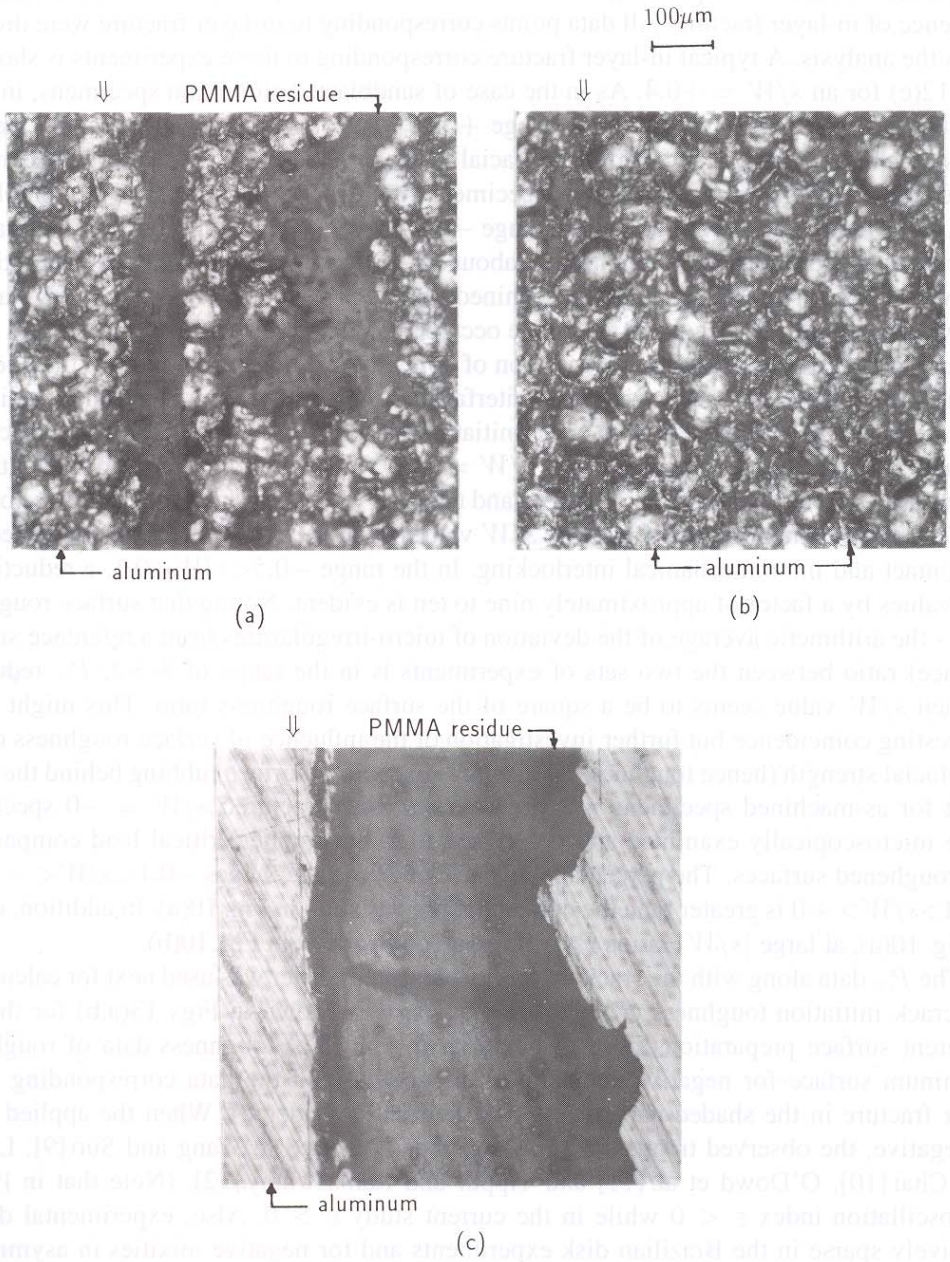

Fig. 12. Micrographs of fractured aluminum surfaces; ⇓ indicates the location of the initial crack front: (a) Roughened surface - in-layer fracture ($s/W = +0.3$), (b) Roughened surface – interfacial fracture ($s/W = -0.2$), (c) As-machined surface – in-layer fracture ($s/W = +0.4$).

toughness is presented. The experiments in this investigation were performed with bimaterial samples prepared from the aluminum half of specimens machined (using the so-called 'fly-cutting' procedure) to produce a relatively smooth (surface roughness factor $R_a \approx 1.4$–1.6) surface. Again several experiments at each value of s/W were performed and the fractured

aluminum surface corresponding to each test was microscopically examined looking for evidence of in-layer fracture. All data points corresponding to in-layer fracture were dropped from the analysis. A typical in-layer fracture corresponding to these experiments is shown in Fig. 12(c) for an $s/W = +0.4$. As in the case of sandblasted aluminum specimens, in-layer fracture occurred more readily in the range $+0.15 < s/W < +0.5$. However, in the case of as-machined surfaces, successful interfacial fracture between PMMA and aluminum was achieved in a small fraction of the test specimens (typically in 20 percent of the samples) at each s/W ratio. On the contrary, in the range $-0.5 < s/W < +0.1$ success rate in obtaining interfacial fracture was relatively higher (about 50–60 percent on average). The variation of P_{cr} with s/W for specimens with as-machined surface is shown in Fig. 10(b). Error bars are shown when multiple successful tests have occured at a s/W value. The overall trends in the critical load at crack initiation as a function of applied load mixity is similar to the one seen in Fig. 10(a). Again, the response of the interfacial system to the sign of the shear acting on the interface plane is different with crack initiation for $s/W = +0$ being lower by a factor of about 1.5 than the one corresponding to $s/W = -0$. One obvious difference between the set of experiments with as-machined surfaces and the ones with roughened surfaces is the overall reduction in the magnitude of P_{cr} for all s/W values as a result of the diminished surface area of contact and micromechanical interlocking. In the range $-0.5 < s/W < 0.1$, a reduction in P_{cr} values by a factor of approximately nine to ten is evident. Noting that surface roughness (R_a – the arithmetic average of the deviation of micro-irregularities from a reference smooth surface) ratio between the two sets of experiments is in the range of 3–3.2, P_{cr} reduction at each s/W value seems to be a square of the surface roughness ratio. This might be an interesting coincidence but further investigation of the influence of surface roughness on the interfacial strength (hence toughness) is needed. Also, crack surface rubbing behind the crack front for as-machined specimens was not obvious when fractured $s/W = -0$ specimens were microscopically examined and could be due to the smaller critical load compared to the roughened surfaces. The percentage increase of P_{cr} in the ranges $-0.1 < s/W < -0$ and $+0.1 > s/W > +0$ is greater than the corresponding variation in Fig. 10(a). In addition, unlike in Fig. 10(a), at large $|s/W|$ ratios P_{cr} values are comparable in Fig. 10(b).

The P_{cr} data along with the crack tip mixity presented earlier was used next for calculating the crack initiation toughness G_{cr}. Plot of G_{cr} vs. $\hat{\psi}$ is shown in Figs. 13(a,b) for the two different surface preparations prior to bonding. In Fig. 13(a) toughness data of roughened aluminum surface for negative values of $\hat{\psi}$ are shown (and the data corresponding to in-layer fracture in the shaded part of Fig. 10(a) are not considered). When the applied shear is negative, the observed trends are similar to those reported in Wang and Suo [9], Liechti and Chai [10], O'Dowd et al. [11] and Tippur and Ramaswamy [12]. (Note that in [9,11], the oscillation index $\varepsilon < 0$ while in the current study $\varepsilon > 0$. Also, experimental data is relatively sparse in the Brazilian disk experiments and for negative mixities in asymmetric bending experiments.) G_{cr} values generally increase at larger negative mixities and values for dominant negative applied shear is about one order higher than the ones corresponding to the smallest overall toughness. Figure 13(b) is the initiation toughness curve for as-machined aluminum surface and the toughness values are shown over the entire range of mixities accomplished in the study. Two orders of magnitude reduction in the toughness values (or by a factor of approximately 100) for comparable phase angles is evident and the ordinates are scaled accordingly in Figs. 13(a,b). Experimental scatter in the data in $G_{cr}(\hat{\psi})$ plots is attributed to the fact that $G_{cr} \propto P_{cr}^2$ at any given s/W. On the whole, G_{cr} vs. $\hat{\psi}$ is asymmetric

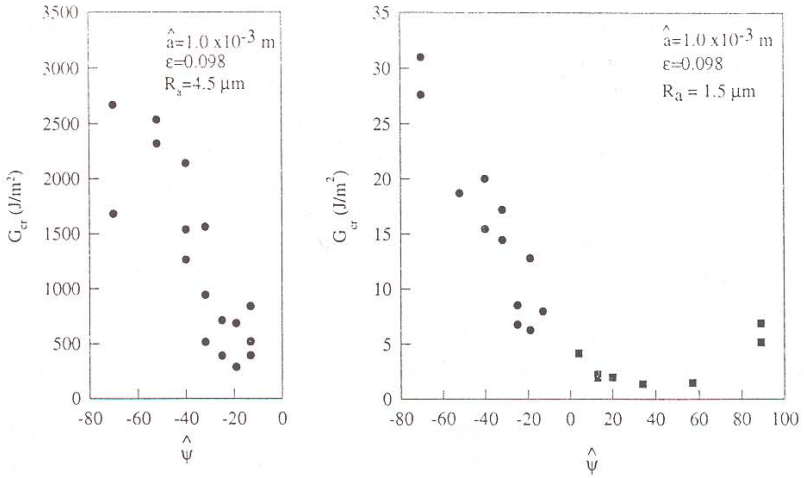

Fig. 13. Energy release rate at crack initiation G_{cr} measured as a function of crack tip mixity. (a) Roughened aluminum surface, (b) As-machined aluminum surface.

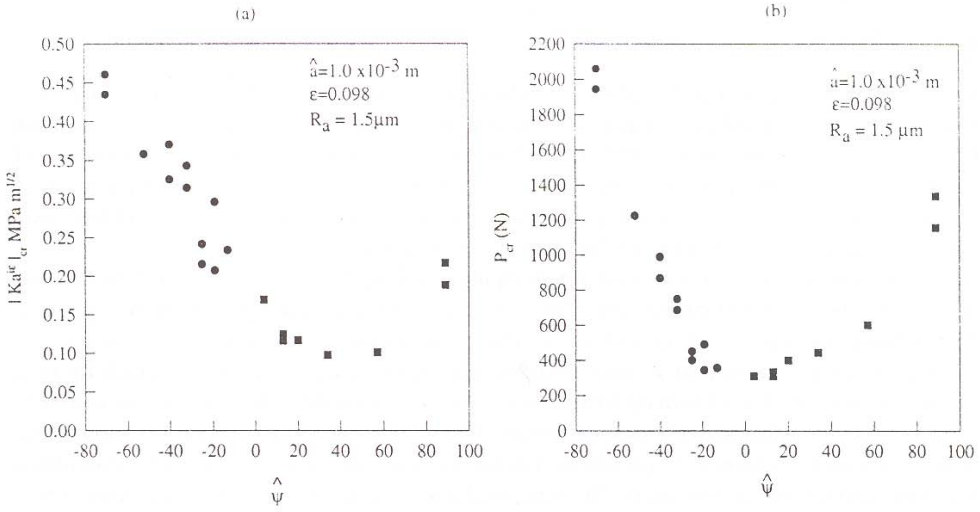

Fig. 14. (a) Dependence of fracture toughness on mixity (notice the different magnitudes of toughness for pure positive and negative shears), (b) Variation of crack initiation strength vs. crack tip mixity for as-machined specimens.

about $\hat{\psi} = 0$ and is similar to other bimaterial systems reported in the literature. $G_{cr}(\hat{\psi})$ curve for this bimaterial system shows that the smallest value of toughness in the range of $30° < \hat{\psi} < 60°$. The crack initiation toughness shows an increasing trend at large values of positive $\hat{\psi}$. *Although the overall variation in the $G_{cr}(\hat{\psi})$ is similar to the one obtained by Liechti and Chai [10], an additional asymmetry in the toughness curve is evident. That is, toughness values for dominant positive shear are much lower than the ones for negative shear acting on the interface. In their study of the influence of plasticity on interfacial fracture toughness, Tvergaard and Hutchinson [30] predict a behavior similar to the one shown in*

Fig. 13(b). Greater asymmetry in toughness curves are predicted for systems when relative tangential displacements of the interface are effectively suppressed in the fracture process zone (Fig. 8(b) of [30]). (Note that in Figs. 8 and 10 in [30], the toughness plots are in terms of critical value of stress intensity factor whereas in Fig. 13 of the present work they are in terms of energy release rate at initiation). For the sake of comparison of the results from this investigation with T&H predictions [30], a plot of the magnitude of critical stress intensity factor $|K\hat{a}^{i\varepsilon}|_{cr}$ vs. mixity $\hat{\psi}$ for as-machined interfaces is shown in Fig. 14(a). Good qualitative agreement between the experimental results and predictions exist. Also, in Fig. 14(b), P_{cr} is plotted as a function of mixity $\hat{\psi}$ which experimentally demonstrates the relationship of the critical applied load P_{cr} with $|K\hat{a}^{i\varepsilon}|$ and hence G_{cr}.

The fracture strength and toughness data in Figs. 13 and 14 suggest that interfacial fracture mechanics analysis can be used for characterizing toughness of bonded joints directly, when surface roughness is relatively small compared to the overall thickness of the interface layer. This is particularly relevant for assessing the fracture toughness of common adhesive joints wherein surface roughening is often suggested for increasing the bond strength. However, it should be noted that in-layer fracture could not be avoided in this investigation when the interface is subjected to positive applied shear.

6. Conclusions

Interface crack tip parameters namely the stress intensity factors and crack tip mixity were measured using CGS and using finite element analysis, independently. A large elastic mismatch bimaterial system consisting of PMMA and aluminum with a material mismatch parameter ε =0.098 was examined. Asymmetric bimaterial four-point-bend specimens with edge cracks cut along interfaces were studied experimentally and numerically while the applied load mixity of shear to normal stress on the interface was varied.

The technique of CGS was used for mapping crack tip fields in the PMMA half of the specimen. The crack tip parameters were extracted from the near tip interference patterns representing interface crack deformation. The contribution of non-singular stresses to the crack tip field was taken into account in the investigation by using asymptotic crack tip field expansion instead of K-dominant terms alone. This improved the experimental measurement of stress intensity factor and crack tip mixity. Complementary finite element computations were performed on identical specimens. Energy release rates and mixities were calculated using interaction integral method. The measured and computed results showed good agreement. The crack tip mixity ψ seems to be linearly related to the applied load mixity Θ for large value of ε.

Fracture tests were conducted using asymmetric four-point-bend specimens under different applied load mixities. Critical fracture loads were measured and energy release rates at crack initiation were calculated. A strong dependence of crack initiation toughness on crack tip mixity was seen. Toughness-mixity data did not show symmetry about any specific mixity value and magnitudes of initiation toughness were different for pure positive and negative shear acting on the interface. The interface toughness for larger negative mixities was approximately an order higher when compared to the smallest toughness. The toughness variation as a function mode-mixity agreed well with the ones predicted by Tvergaard and Hutchinson who have considered the influence of crack tip plasticity on interfacial fracture toughness in their analysis. Also, the experiments on two different surface roughnesses prior to bonding have suggested a roughness induced fracture toughness enhancement.

Acknowledgments

The support for the research through NSF RIA MSS9109731 and NSF Grant MSS9313153 is greatly appreciated.

References

1. J.R. Rice, *Journal of Applied Mechanics* 55 (1988) 98–103.
2. J.W. Hutchinson and Z. Suo, *Advances in Applied Mechanics* 29 (1991) 63–191.
3. M.L. Williams, *Bulletin of the Seismological Society of America* 49(2), (1959) 199–203.
4. G.C. Sih and J. R. Rice, *Journal of Applied Mechanics* 32 (1965) 418–423.
5. F. Erdogan, *Journal of Applied Mechanics* 32 (1965) 403–410.
6. B.M. Malyshev and R.L. Salganik, *International Journal of Fracture* 1 (1965) 114–12.
7. M. Comninou, *Journal of Applied Mechanics* 44 (1977) 631–636.
8. H.C. Cao and A.G. Evans, *Mechanics of Materials* (1989) 295–301.
9. J.-S. Wang and Z. Suo, *Acta Metallurgica* 38(7), (1990) 1279–1290.
10. K.M. Liechti and Y.S. Chai, *Journal of Applied Mechanics* 58 (1991) 680–687.
11. N.P. O'Dowd, M.G. Stout and C.F. Shih, *Philosophical Magazine A* 66(6), (1992) 1037–1064.
12. H.V. Tippur and S. Ramaswamy, *International Journal of Fracture* 61 (1993) 247–265.
13. J.G. Williams, *International Journal of Fracture* 36 (1988) 101–119.
14. N.P O'Dowd, C.F. Shih and M.G. Stout, *International Journal of Solids and Structures* 29(5), (1992) 571–589.
15. P.G. Charalambides, J. Lund and A.G. Evans *Journal of Applied Mechanics* 56 (1989) 77–82.
16. H. Lu and F.P. Chiang, *Journal of Applied Mechanics* 60 (1993) 93–100.
17. H.V. Tippur and A.J. Rosakis, *Experimental Mechanics* 31(3), (1991) 243–252.
18. K.M. Liechti and W.G. Knauss, *Experimental Mechanics* 22 (1982) 383–391.
19. M. Charalambides, A.J. Kinloch, Y. Wang and J.G. Williams, *International Journal of Fracture* 54 (1992) 269–291.
20. S. Suresh, C.F. Shih, A. Morrone and N.P. O'Dowd, *Journal of the American Ceramic Society* 73 (1990) 1257–1267.
21. C.F. Shih and R. Asaro, *Journal of Applied Mechanics* 55 (1988) 299–316.
22. H.V. Tippur, S. Krishnaswamy and A.J. Rosakis, *International Journal of Fracture* 52 (1991) 91–117.
23. H.V. Tippur, *Applied Optics* 33 (1994) 4167–4170.
24. Ibid, 31 : 2 (1992) 4428–4439.
25. Y.J. Lee and A.J. Rosakis, *International Journal of Solids and Structures* 30(22), (1993) 3139–3158.
26. S. Ramaswamy, H.V. Tippur and L. Xu, *Experimental Mechanics* 33(3), (1993) 218–227.
27. M.Y. He and J.W. Hutchinson, *Journal of Applied Mechanics* 56 (1989) 270.
28. M. Comninou and D. Schmueser, *Journal of Applied Mechanics* 46 (1979) 345–348.
29. A.G. Evans and J.W. Hutchinson, *Acta Metallurgica* 37 (1989) 909–916.
30. V. Tvergaard and J.W. Hutchinson, *Journal of the Mechanics and Physics of Solids* 41(6) (1993) 1119–1135.